Dalton Transactions

ROYAL SOCIETY OF CHEMISTRY

PAPER

View Article Online
View Journal | View Issue

Cite this: *Dalton Trans.*, 2020, **49**, 15731

H-shaped oxalate-bridging lanthanoid-incorporated arsenotungstates†

Hanhan Chen, Zikang Xiao, Bing Yan, Hechen Wu, Pengtao Ma, * Jingping Wang and Jingyang Niu *

Received 10th August 2020,
Accepted 9th October 2020

DOI: 10.1039/d0dt02792h

rsc.li/dalton

Three oxalate-bridging lanthanide-based polyoxometalates (Ln-POMs) $K_{17}Na_2H_5[\{(As_2W_{19}O_{67}(H_2O))Ln(H_2O)_2\}_2(C_2O_4)]\cdot 50H_2O$. [Ln = Sm^{3+} (**1**), Pr^{3+} (**2**), and Ce^{3+} (**3**)] were successfully synthesized. The structures were further characterized by single-crystal X-ray diffraction analyses, Raman spectroscopy, elemental analyses, powder X-ray diffraction (PXRD), IR spectra, UV/vis diffuse reflectance spectroscopy, and thermogravimetric analysis (TGA). The structural characterization study reveals that Ln-POMs **1–3** crystallize in the form of the triclinic space group $P\bar{1}$ and consist of an oxalate bridging di-Ln^{3+}-incorporated H-shaped dimer, which can also be viewed as a combination of two half-units $\{Ln(As_2W_{19}O_{67}(H_2O))(H_2O)_2\}_2^{22-}$ related by an inversion center. It is worth noting that the opening angle (33.01°) from the $[As_2W_{19}O_{67}(H_2O)]^{14-}$ fragment in **1–3** is less than that of the $[As_2W_{19}O_{67}(H_2O)]^{14-}$ precursor (40.99°). Furthermore, the stability of **1–3** in aqueous solution and their solid-state photoluminescence properties have also been investigated in this work.

Introduction

Polyoxometalates (POMs), as a rich class of discrete anionic early-transition-metal–oxide building blocks mainly based on V^{5+}, Nb^{5+}, Mo^{6+} or W^{6+}, possess a variety of chemical structures.[1] Their chemical and physical properties can be readily modulated by tuning their different components, including but not limited to metal ions and organic functional ligands.[2] For example, lacunary POMs, where one or multiple $\{MO_x\}$ units are removed, anchor almost all of their elements at their vacant sites, thus generating special new POMs with diverse bonding patterns and electronic configurations. Consequently, POMs exhibit extensive applications in various fields, such as magnetism, catalysis, optics, medicine, *etc.*[3] Lanthanoid (Ln^{3+}) cations are highly reactive to the POM ligands owing to their high coordination numbers and large oxophilicity, as a result, forming Ln-substituted POMs (Ln-POMs).[4] Since the advent of the first Ln-POMs by Peacock and Weakley in 1971, a large number of Ln-POMs have been reported and widely studied in optics, catalysis, and magnetic fields.[5] Especially the hybrid Ln-POMs functionalized by organic conjugated ligands, have greatly attracted research attentions worldwide.[6] In such systems, POMs and organic ligands absorb light and transport energy to Ln^{3+} *via* intermolecular energy transfer.[7] This unique multi-component luminescent organic–inorganic hybrid Ln-POM opens a new avenue in the exploration and discovery of novel luminescence materials. In this field, Zhao's group has conducted intensive research studies on synthesizing novel organic–inorganic hybrid Ln-POM materials and successfully reported the photoluminescence (PL) results of several species.[8] Meanwhile, our group has also made progress in exploring organic–inorganic hybrid Ln-POM compounds with novel properties.[9]

Arsenotungstates (ATs), an important subfamily of POMs, have attracted increasing interest over several decades. Specifically, Boskovic and colleagues have made significant contributions to the field of organic-ligand-functionalized Ln-containing ATs.[10] In 2010, they discovered two structurally related polynuclear Tb^{3+}-based ATs $[Tb_2(pic)(H_2O)_2(B\text{-}\beta\text{-}AsW_8O_{30})_2(WO_2(pic))_3]^{10-}$ and $\{Tb_8(pic)_6(H_2O)_{22}(B\text{-}\beta\text{-}AsW_8O_{30})_4[WO_2(pic)]_6\}^{12-}$ for the first time, and demonstrated the luminescence sensitization of organic ligands.[10a] Two years later, they studied the luminescence characteristics of different Tb^{3+} centers with site specificity and photosensitization using organic and/or inorganic ligands.[10b] Those compounds were synthesized by the reactions of the lacunary AT precursor $[As_2W_{19}O_{67}(H_2O)]^{14-}$ (As_2W_{19}),[11] Ln^{3+} cations and carboxylic acid in deionized water. Notably, the As_2W_{19} precur-

Henan Key Laboratory of Polyoxometalate Chemistry, College of Chemistry and Chemical Engineering, Henan University, Kaifeng, Henan 475004, P. R. China. E-mail: mpt@henu.edu.cn, jyniu@henu.edu.cn; Fax: +86-371-23886876

†Electronic supplementary information (ESI) available: Material and physical measurements, X-ray crystallography, relevant structural tables, PXRD, TGA curves, IR spectra, liquid phase Raman spectra of **2–3**. CCDC 2018536–2018538. For ESI and crystallographic data in CIF or other electronic format see DOI: 10.1039/D0DT02792H

sor, as a metastable AT, could be reorganized into new structural architectures in solution. Therefore, a large number of AT derivatives with novel structures have been constructed as of today, displaying many interesting chemical and physical properties, for example, photochromism, photoemission, and single-molecule magnet behaviors.[12] Some benchmarks are worth mentioning here: $[As^{III}_6W_{65}O_{217}(H_2O)_7]^{26-}$ (ref. 11*b*) and $[Gd_8As_{12}W_{124}O_{432}(H_2O)_{22}]^{60-}$ (ref. 12*a*) represent the largest ATs to be made so far. The 1-D infinite helical chain-like organic–inorganic hybrid AT, $Na_4H_8[\{Pr(H_2O)_2\}_2\{As_2W_{19}O_{68}\}\{WO_2(mal)\}_2]\cdot 24H_2O$, displays excitation wavelength-dependent emission behaviours and reversible green-orange-yellow luminescence switching phenomenon[9*d*] and $[Er_3(\mu_3\text{-}OH)(H_2O)_8(AsW_9O_{33})(AsW_{10}O_{35}(DL\text{-}mal))]_2^{22-}$ has been reported to exhibit magnetic field-induced two-step relaxation.[12*b*]

In our previous work, we have developed a POM synthesis protocol achieving the assembly of As_2W_{19} precursor and Ln^{3+} cations assisted by well-selected carboxylic acid ligands. Using a similar approach, a family of dermic H-shaped oxalate-bridging Ln-substituted ATs $K_{17}Na_2H_5[\{(As_2W_{19}O_{67}(H_2O))Ln(H_2O)_2\}_2(C_2O_4)]\cdot 50H_2O$ (Ln = Sm^{3+} (**1**), Pr^{3+} (**2**), and Ce^{3+} (**3**)) were isolated, which were determined by X-ray single-crystal diffraction and further characterized by elemental analysis, thermogravimetric analyses (TGA) (Fig. S1†), powder X-ray diffraction (PXRD), UV/vis diffuse reflectance spectroscopy, Raman spectroscopy, and IR spectra. Furthermore, the solid-state PL properties of **1–3** were also studied at room temperature.

Results and discussion

Crystal structure

The PXRD patterns (Fig. S2†) and crystallographic parameters of the samples confirm that **1–3** are isomorphic and crystallize in the triclinic space group $P\bar{1}$ (Table S1†). The polyanion skeletons of isostructural **1–3** exhibit a dimeric polyanion $[\{(As_2W_{19}O_{67}(H_2O))Ln(H_2O)_2\}_2(C_2O_4)]^{24-}$, which was mainly assembled from two As_2W_{19} building blocks related by two Ln^{3+} cations and one oxalate ligand. So we take the $[\{(As_2W_{19}O_{67}(H_2O))Sm(H_2O)_2\}_2(C_2O_4)]^{24-}$ polyanion as an example to illustrate its structure. Bond valence sum (BVS) calculations[13] indicate that all As, W, and Sm centers are +3, +6, and +3, respectively (Table S2†). The polyanion $[\{(As_2W_{19}O_{67}(H_2O))Sm(H_2O)_2\}_2(C_2O_4)]^{24-}$ (Fig. 1a) can be divided into two dilacunary As_2W_{19} fragments combined together by an oxalate ligand and di-Sm^{3+}. These fragments can also be regarded as a combination of two half-units $[\{(As_2W_{19}O_{67}(H_2O))Sm(H_2O)_2\}^{11-}$ with idealized C_{2V} symmetry (Fig. 1b).

The As_2W_{19} fragment remains essentially unchanged; every As atom inhabits a tri-coordinate environment and is built by three μ_4-O atoms from three $\{W_3O_{13}\}$ building blocks with As–O distances of 1.79(11)–1.81(12) Å (Tables S3†). To date, the ATs containing a relatively intact As_2W_{19} skeleton have rarely been reported.[14] Nevertheless, the As1–As2 distance (6.132(3) Å) in **1** is significantly shorter than that of 6.522(11) Å in the As_2W_{19} precursor, and the opening angle of 33.01° of

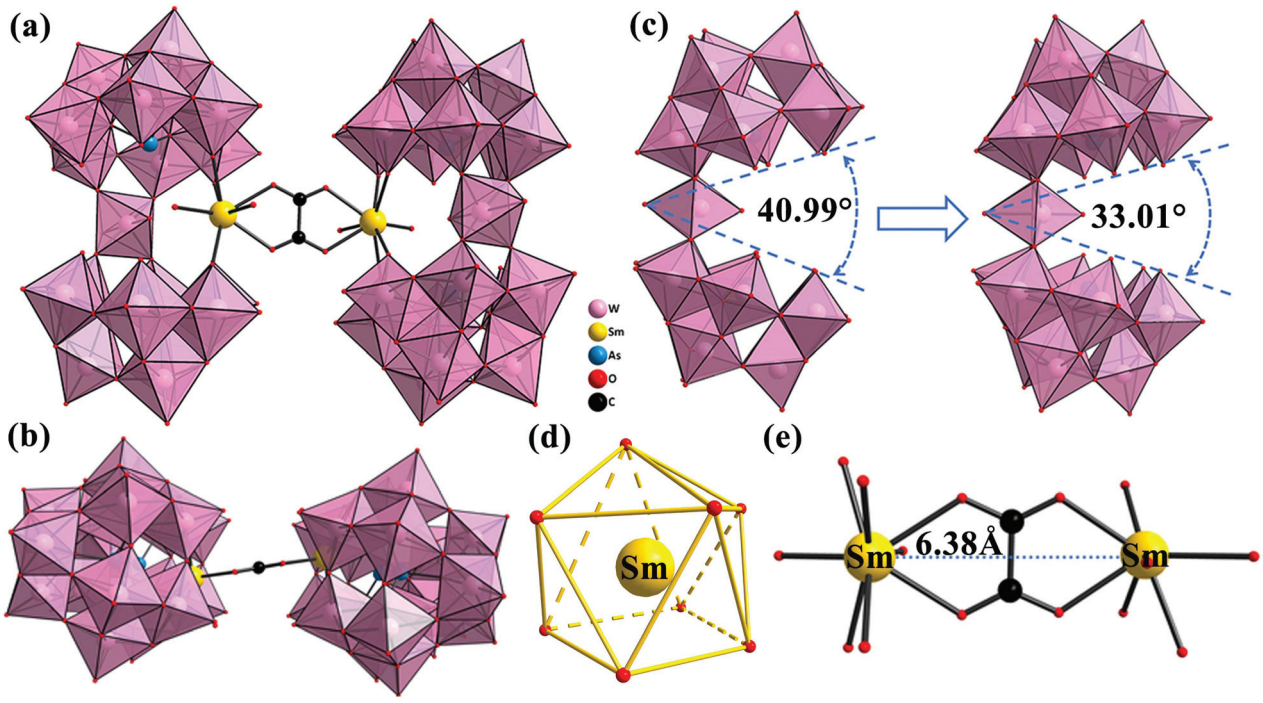

Fig. 1 (a) Polyhedral/ball-and-stick representation of the polyanion in **1**; (b) polyhedral representation of **1** (top view); (c) the polyhedral representation of the precursor $[As_2W_{19}O_{67}(H_2O)]^{14-}$; the polyhedron representation of the variable $[As_2W_{19}O_{67}(H_2O)]^{14-}$ unit in **1**; (d) bi-augmented trigonal prism J50 geometry of the Sm^{3+} cations; and (e) coordination mode of the Sm^{3+} cations and oxalate ligand. All the hydrogen atoms and crystal water molecules have been omitted for clarity (W, rose; O, red; Sm, yellow; As, turquoise; C, black; $\{WO_6\}$, rose).

As_2W_{19} fragments in **1** is distinctly less than that of the As_2W_{19} raw material (40.99°) (Fig. 1c). To the best of our knowledge, it may be caused by the fact that Sm^{3+} cations are strongly bound to four neighboring W atoms from two $[AsW_9O_{33}]^{9-}$ building blocks through oxygen bridges. As a result, the adjacent $[AsW_9O_{33}]^{9-}$ building blocks are strongly bound *via* the W–O–Sm–W–O linker, resulting in a much smaller opening angle. SHAPE 2.1 software was used for continuous-shape measure analysis of Sm^{3+} cations.[15] The eight-coordinate Sm^{3+} cations exhibit a bi-augmented trigonal prism (C_{2v}) geometry (Fig. 1d, Tables S4 and S5†), being surrounded by four O atoms of four {WO_6} units, respectively; two O atoms originated from the two water molecules and the other two O atoms from the oxalate ligand. The oxalate ligand as a tetradentate ligand chelates two Sm^{3+} cations (with the Sm···Sm distance of 6.38(3) Å), thus forming double five-membered rings of Sm–O–C–C–O (Table S6†). Therefore, the oxalate ligand plays a crucial role in the stabilization of the integral skeleton (Fig. 1e). In addition, **1** displays an oxalate bridging di-Sm^{3+}-substituted H-shaped dimeric structure, and the adjacent dimeric polyanions are regularly stacked in the –AAA– arrangement. It is interesting that adjacent $[\{(As_2W_{19}O_{67}(H_2O))Sm(H_2O)_2\}_2(C_2O_4)]^{24-}$ polyanions are distributed along the *b* axis in a staggered pattern to reduce the steric hindrance (Fig. 2). This reminds us of another two kinds of oxalate-bridging Ln-substituted Keggin-type phosphotungstates, $\{[(\alpha\text{-}PW_{11}O_{39})Ln(H_2O)]_2(C_2O_4)\}^{10-}$ (Ln = Y^{3+}, Dy^{3+}, Ho^{3+}, Er^{3+}) and $\{(\alpha\text{-}x\text{-}PW_{10}O_{38})Tm_2(C_2O_4)(H_2O)_2\}^{3-}$.[16] $\{[(\alpha\text{-}PW_{11}O_{39})Ln(H_2O)]_2(C_2O_4)\}^{10-}$ (Fig. S3a†) represents a dimeric mono-Ln substituted phosphotungstate, which consists of two Keggin-type $[Ln(\alpha\text{-}PW_{11}O_{39})]_2^{14-}$ subunits linked by one oxalate ligand.[16a] The dimeric $\{(\alpha\text{-}x\text{-}PW_{10}O_{38})Tm_2(C_2O_4)(H_2O)_2\}_2^{6-}$ (Fig. S3b†) is constructed by two $[Tm_2(\alpha\text{-}x\text{-}PW_{10}O_{38})]^{5-}$ linked *via* the oxalate ligands.[16a] In addition, Zhao's group obtained three series of oxalate functionalized Ln-based phosphotungstates, $[Ln_2(H_2ox)_2(ox)(\alpha_2\text{-}P_2W_{17}O_{61})_2]^{16-}$ (Ln = Ho^{3+}, Er^{3+}, Tm^{3+}, Yb^{3+}, Y^{3+}; H_2ox = oxalic acid), $[Ln_2(C_2O_4)(H_2O)_4(OH)W_4O_{16}]_2^{10-}$, and $[Ln(C_2O_4)W_5O_{18}]_4^{20-}$ (Ln = Eu^{3+}, Ho^{3+}, Er^{3+}, or Tb^{3+}).[16b,c] The S-shaped polyanion $[Ln_2(H_2ox)_2(ox)(\alpha_2\text{-}P_2W_{17}O_{61})_2]^{16-}$ (Fig. S3c†) is made up of two mono-Ln substituted Dawson-type $[Ln(H_2ox)(\alpha_2\text{-}P_2W_{17}O_{61})]^{7-}$ subunits linked together through a $C_2O_4^{2-}$ bridge.[16b] A centrosymmetric dimeric phosphotungstate $[Ln_2(C_2O_4)(H_2O)_4(OH)W_4O_{16}]_2^{10-}$ (Fig. S3d†) can be viewed as a combination of two di-Ln^{3+}-substituted Lindqvist segments *via* two oxalate linkers. The most remarkable feature in the dimer is that two Ln^{3+} clusters are linked together through two tetradentate oxalates giving rise to a rectangular tetra-Ln^{3+} cluster.[16c] Different from $[Ln_2(C_2O_4)(H_2O)_4(OH)W_4O_{16}]_2^{10-}$, $[Ln(C_2O_4)W_5O_{18}]_4^{20-}$ (Fig. S3e†) is composed of four mono-Ln^{3+}-substituted Lindqvist segments with four oxalate connectors, in which the monolacunary Lindqvist $[W_5O_{18}]^{6-}$ subunit originates from the removal of a W=O group from the $[W_6O_{19}]^{2-}$ matrix.[16c]

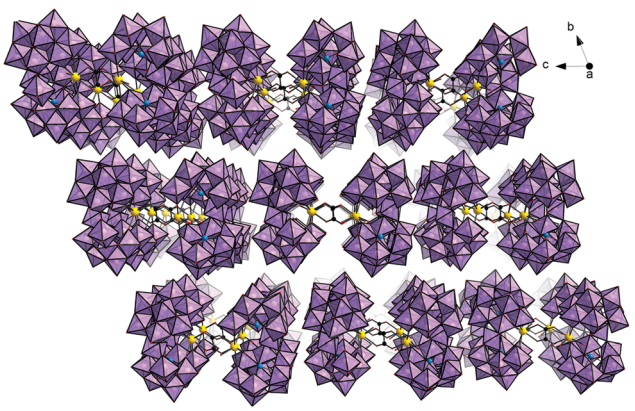

Fig. 2 The 3-D packing of $[\{(As_2W_{19}O_{67}(H_2O))Sm(H_2O)_2\}_2(C_2O_4)]^{24-}$ units in **1** viewed along the *a* axis.

IR spectra

The existence of the polyoxotungstate clusters and oxalate ligands in the crystalline solids **1–3** is confirmed by IR spectra (Fig. S4†). In the high-frequency region, the spectra of **1–3** are dominated by an intense and wide absorption peak at 3432–3446 cm^{-1}, which arises from the ν(O–H) stretching mode of the water molecules.[9c] For the coordination modes of the carboxylate group, the difference ($\Delta\nu = \nu_{asym} - \nu_{sym}$) between the asymmetric (ν_{asym}) and symmetric (ν_{sym}) stretching vibrations is commonly used and the $\Delta\nu$ values indicate the presence of bridging coordination mode for the oxalate ligand.[17] As a result, the strong absorption band at 1643 cm^{-1} can be viewed as the asymmetric stretching vibration of the carboxylic group, while the absorption band at 1320 cm^{-1} corresponds to the symmetric stretching vibration of the carboxylic group.[17a] In comparison with the free oxalate ligand (the asymmetric and symmetric stretching vibrations are observed at 1690 and 1350 cm^{-1}), these bands shifted to lower wavenumbers for compound **1**, thus indicating that the oxalate ligands were coordinated to the Ln^{3+} cations.[17b] In the region of 1000–650 cm^{-1}, **1–3** display four characteristic vibration patterns, namely ν(W–O_d), ν(As–O_a), ν(W–O_b), and ν(W–O_c) that are derived from the W–O skeleton and As–Oa, respectively, and appear at 947, 885, 795, and 733 cm^{-1}, respectively.[17c]

Raman spectroscopy

The high sensitivity of the IR spectra to the changes in dipole moment can generate strong signals from the water and hydroxyl groups, but no signal from diatomic molecules without dipole moment. In contrast, Raman spectroscopy can detect diatomic molecules, although it has low sensitivity for the changes in dipole moment.[18] A significant result of these vibrational selection rules is that Raman spectroscopy can monitor the vibrations of aqueous phases, while IR spectroscopy is not able to due to the strong absorption of the IR signal by the aqueous phase.[18a] Based on the above conclusions, to better understand the solution properties of **1–3** toward deionized water, Raman spectroscopy measurements in aqueous solution were performed. The Raman spectra of

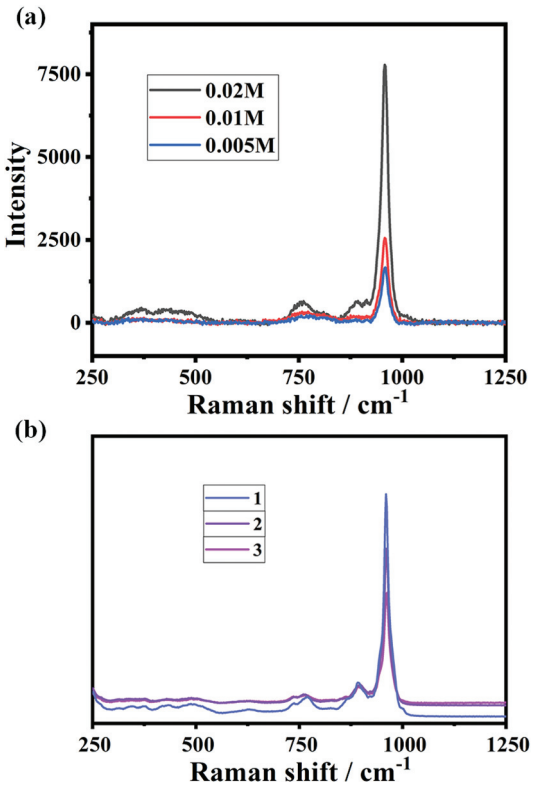

Fig. 3 (a) **1** dissolved in deionized water at different concentrations *i.e.*, 2×10^{-2} M, 1×10^{-2} M, and 5×10^{-3} M; and (b) solid-state Raman spectra of **1–3**.

1–3 in aqueous solutions were measured at three concentrations *i.e.*, 2×10^{-2} M, 1×10^{-2} M, and 5×10^{-3} M (Fig. 3a, Fig. S5 and S6†). In the 250–1250 cm^{-1} range, the characteristic of Raman peaks for **1** is in good agreement with those recorded for the solid phase (Fig. 3b).[18b] In this concentration range, no extra signals were observed, manifesting no partial degradation in aqueous solutions. The obvious feature bands that appeared in the Raman spectroscopy of the POM skeleton come from the ν(W–O_t) 959 cm^{-1}, ν(W–O_b) (895 and 861) cm^{-1} and ν(W–O_c) (767 and 735) cm^{-1} vibrations.

UV/vis diffuse reflectance spectroscopy

The diffuse reflectivity for solid samples of compounds **1–3** was performed at 200–800 nm at room temperature (Fig. 4). All the samples of **1–3** displayed an absorption band around 328 nm, which is assigned to the p_π–d_π charge-transfer transitions of the O → W bonds.[19] **1** exhibits five bands at 402, 417, 438, 460 and 476 nm, assigned to the $^6H_{5/2} \rightarrow {}^4F_{7/2}$, $^6H_{5/2} \rightarrow {}^6P_{9/2}$, $^6H_{5/2} \rightarrow {}^4G_{9/2}$, $^6H_{5/2} \rightarrow {}^4I_{13/2}$, and $^6H_{5/2} \rightarrow {}^4I_{11/2}$ f–f transitions, respectively.[20] Differently, the UV/vis diffuse reflectance spectrum of **2** displays four sharp absorption bands at 446, 470, 483 and 591 nm, resulting from the $^3H_4 \rightarrow {}^3P_2$, $^3H_4 \rightarrow {}^3P_1$, $^3H_4 \rightarrow {}^3P_0$ and $^3H_4 \rightarrow {}^7D_2$ transitions of the Pr^{3+} cations, respectively. In addition, the broad absorption band at around 470 nm could be found in the UV/vis diffuse reflectance spectrum of **3** and this may be due to the allowed

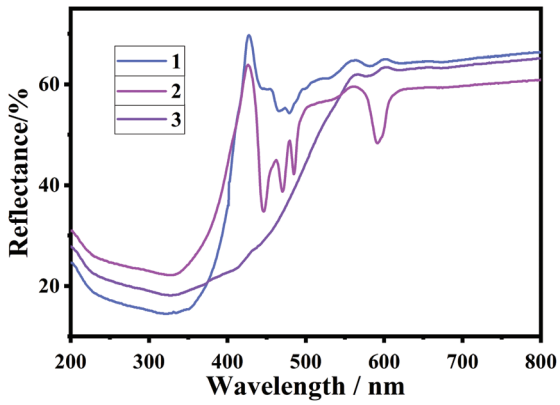

Fig. 4 The UV/vis diffuse reflectance spectra of **1–3**.

4f → 5d electron transition of the Ce^{3+} cations, demonstrating the presence of the Ce^{3+} cations in **3**.[18b]

Photoluminescence properties

Ln^{3+} cations possess outstanding photophysical properties, including sharp and characteristic transitions in the visible or near-infrared regions and long emission lifetime scale. Therefore, the PL properties of the Ln^{3+} cations have attracted increasing interest for several decades and have evoked great interest in cathode ray tubes, light-emitting diodes, fluorescent tubes, bio-analysis and imaging devices.[21] In Ln-POM compounds, the POM segments can be considered as suitable sensitizers. Upon photoexcitation, they act as antenna ligands to transfer energy from the O → M ligand to the metal charge transfer state.[10b,22] Herein, the solid-state PL of **1** was carried out at room temperature. As shown in Fig. 5a,† the excitation spectrum of **1** was recorded on the emission at 599 nm. The excitation spectrum displays a strong broad band varying from 400 nm to 450 nm with maximum *ca.* 432 nm mainly corresponding to the $^1A_{1g} \rightarrow {}^1T_{1u}$ transition originating from the ATs and two obvious f–f excitation peaks at 378 and 391 nm, respectively, ascribed to the $^6H_{5/2} \rightarrow {}^4L_{15/2}$ and $^6H_{5/2} \rightarrow {}^6P_{7/2}$ transitions of Sm^{3+}. In light of the excitation spectrum, the emission spectrum of **1** was recorded at the excitation wavelength of 432 nm. Five emission peaks can be noticed at 495, 561, 599, 646 and 705 nm in the emission spectrum of **1** (Fig. 5b). To further explore the origins of the broad emission from 450 nm to 550 nm, the emission spectra of the As_2W_{19} precursor were recorded at the excitation wavelength of 432 nm under the same experimental conditions. The emission position (Fig. 5b) of the As_2W_{19} material is the same as that of **1**, which displays the broad emission centered at 495 nm primarily derived from the AT segments. The other four peaks at 564, 599, 646 and 705 nm could be attributed to the characteristic $^4G_{5/2} \rightarrow {}^6H_{5/2}$, $^4G_{5/2} \rightarrow {}^6H_{7/2}$, $^4G_{5/2} \rightarrow {}^6H_{9/2}$ and $^4G_{5/2} \rightarrow {}^6H_{11/2}$ transitions of Sm^{3+}.[8d,22a] It is well known that both magnetic-dipole and electric-dipole transitions exist together in the characteristic f–f transitions of Ln^{3+}.[6b] Generally, the magnetic-dipole $^4G_{5/2} \rightarrow {}^6H_{5/2}$ emission inten-

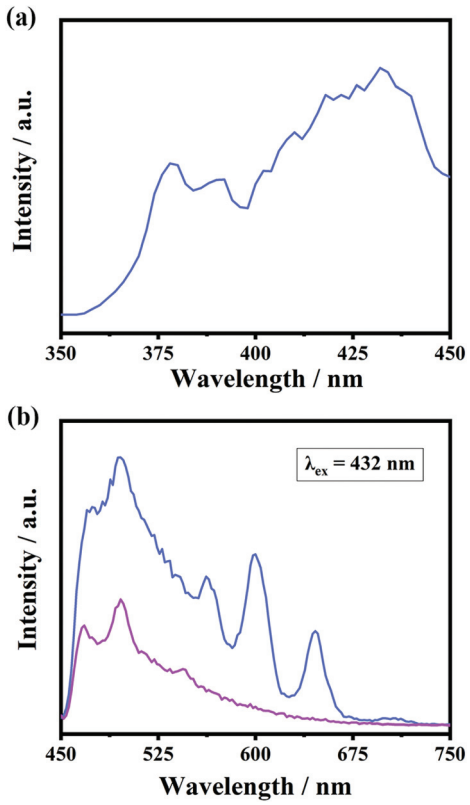

Fig. 5 (a) The excitation spectrum of **1** recorded under emission at 599 nm; and (b) the emission spectrum of **1** (blue solid line) and $K_{14}[As_2W_{19}O_{67}(H_2O)]$ precursor (purple solid line) under excitation at 432 nm.

sity hardly changes with the coordination environment of the Sm^{3+} cation, whereas the electric-dipole $^4G_{5/2} \rightarrow {}^6H_{9/2}$ emission intensity is highly influenced by the local environment. Thus, the $I(^4G_{5/2} \rightarrow {}^6H_{9/2})/I(^4G_{5/2} \rightarrow {}^6H_{5/2})$ intensity ratio often functions as an indicator of the symmetry of the local environment of the Sm^{3+} cation.[22a,b] The $I(^4G_{5/2} \rightarrow {}^6H_{9/2})/I(^4G_{5/2} \rightarrow {}^6H_{5/2})$ intensity ratio for **1** of 1.148 : 1 indicates that the Sm^{3+} cations exist in the low-symmetric coordination environments, which is consistent with the eight-coordinate biaugmented trigonal prism geometry of the Sm^{3+} cations from the single crystal X-ray diffraction analysis. The decay lifetime curves of **1** under the conditions of the strongest emission at λ = 599 nm and excitation at 432 nm can be fitted with the second-order exponential function $I = A_1 \exp(-t/\tau_1) + A_2 \exp(-t/\tau_2)$ (where τ_1 and τ_2 = fast and slow components of the luminescence lifetimes, respectively, and A_1 and A_2 = pre-exponential factors). The fitting lifetimes are of the values τ_1 = 9.25 μs and τ_2 = 32.62 μs (Fig. S7†). From the structural analysis of **1**, two Sm^{3+} ions reside in the same coordination environment, meaning that the lifetime-decay curve should follow the single exponential equation. However, this case is not in conformity with the experimental result of **1**. We speculate that there is a non-ignorable effect from the fast lifetime decay of AT components in **1**, as observed in the previous literature.[22]

With the purpose of demonstrating the energy transfer (ET) process from the AT segments to the Sm^{3+} cations in **1**, time-resolved emission spectra (TRES) of **1** under excitation at 402 nm were recorded in the range of 420–750 nm (Fig. 6). Initially, the intensity of the broad emission band at *ca.* 450 nm ($^3T_{1u} \rightarrow {}^1A_{1g}$ emission band) increases from 18.0 μs and reaches the maximum at 20.0 μs. As time elapses, the intensity of the $^3T_{1u} \rightarrow {}^1A_{1g}$ emission band constantly falls. Simultaneously, the intensities of the f–f emission peaks from the Sm^{3+} center increase and reach the maximum at *ca.*

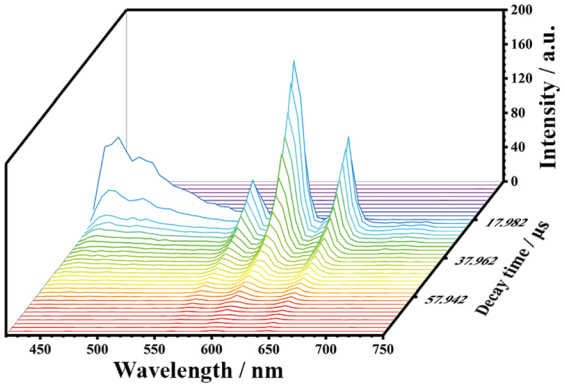

Fig. 6 TRES spectra of **1** under the excitation at 402 nm.

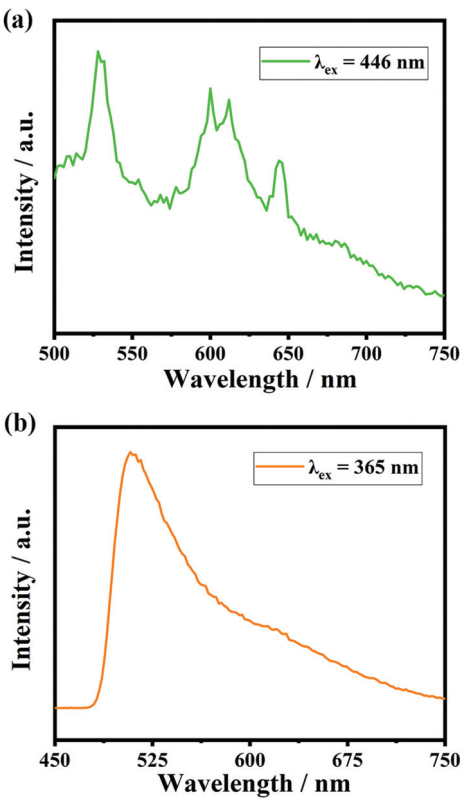

Fig. 7 The emission spectrum of **2** (a) and **3** (b) recorded under excitation at 446 and 365 nm, respectively.

22.0 μs, which unambiguously consolidate that ET occurs from AT segments to Sm^{3+} cations. Until 32.0 μs, the $^3T_{1u} \rightarrow {}^1A_{1g}$ emission band at *ca.* 450 nm disappears and the intensities of the emission peaks at 564, 599, 646 and 705 continually decline, indicating that the ET process from AT segments to Sm^{3+} emission centers has been accomplished (Fig. S8†).

According to the results of the diffuse reflectance spectra of **2** and **3**, the emission spectra of **2** and **3** (Fig. 7) were recorded under a maximum excitation at 446 nm and 365 nm, respectively. The emission spectrum (Fig. 7a) of **2** displays five prominent f–f emitting peaks at 528, 600, 612, 645 and 686 nm, which are assigned to the $^3P_1 \rightarrow {}^3H_5$, $^1D_2 \rightarrow {}^3H_4$, $^3P_0 \rightarrow {}^3H_6$, $^3P_0 \rightarrow {}^3F_2$ and $^3P_1 \rightarrow {}^3F_2$ transitions of Pr^{3+} cations, respectively. The monitoring of the luminescent-decay curve of the emission at 528 nm ($^3P_1 \rightarrow {}^3H_5$) can be fitted to a second-order exponential function, thus giving τ_1 = 1.01 μs and τ_2 = 8.08 μs (Fig. S9†). However, the emission spectrum (Fig. 7b) of **3** shows one abroad band at 508 nm, which can be contributed to the $^3T_{1u} \rightarrow {}^1A_{1g}$ transitions of O → W ligand to metal charge transfer of the AT constituents. No characteristic emissions of the Ce^{3+} cations appeared in the spectrum of **3**; possibly, the emissions of ATs completely covered the much lower 5d → 4f transition of the Ce^{3+} cations.[18b] In addition, under the strongest 508 nm emission and the 365 nm excitation, (Fig. S10†), the lifetime decay curve of **3** can be fitted to a double exponential function, yielding two luminescence lifetimes of 1.28 μs for τ_1 and 8.00 μs for τ_2. This is consistent with the previously reported literature.[22b]

Conclusion

In conclusion, a class of novel organic–inorganic hybrid Ln-POM $K_{17}Na_2H_5[\{(As_2W_{19}O_{67}(H_2O))Ln(H_2O)_2\}_2(C_2O_4)]\cdot 50H_2O$ [Ln = Sm^{3+} (**1**), Pr^{3+} (**2**), and Ce^{3+} (**3**)] were successfully synthesized under hydrothermal conditions and were well characterized by several physicochemical technologies. The structural analyses indicate that compounds **1–3** are composed of oxalate bridging di-Ln^{3+}-substituted H-shaped dimers, which could also be viewed as a combination of two half-units $\{(As_2W_{19}O_{67}(H_2O))Ln(H_2O)_2\}_2^{11-}$ related by an inversion center. The $[As_2W_{19}O_{67}(H_2O)]^{14-}$ fragment remains essentially unchanged; however, the opening angle (33.01°) of $[As_2W_{19}O_{67}(H_2O)]^{14-}$ fragments in **1** is less than that of $[As_2W_{19}O_{67}(H_2O)]^{14-}$ in the precursor (40.99°) because of the tractive force of Ln^{3+} cation insertion. The liquid phase Raman spectra of **1–3** are consistent with those recorded in the solid phase within the 250–1250 cm^{-1} range, indicating the integrity of compounds **1–3** in deionized water. In addition, the PL spectra and lifetime behaviors of **1–3** have also been explored. Furthermore, the TRES spectra of **1** demonstrate the energy transport from the As_2W_{19} segment to the Sm^{3+} centers during the course of photoluminescence. With that, we hope the discovery of organic–inorganic hybrid Ln-POM **1–3** could enrich the Ln-POM family and contribute towards developing more novel Ln-based luminescent materials.

Experimental

Syntheses of $K_{17}Na_2H_5[\{(As_2W_{19}O_{67}(H_2O))Sm(H_2O)_2\}_2(C_2O_4)]\cdot 50H_2O$ (1)

$SmCl_3\cdot 6H_2O$ (0.091 g, 0.25 mmol), $K_{14}[As_2W_{19}O_{67}(H_2O)]$ precursor (0.66 g, 0.125 mmol) and oxalate (0.066 g, 0.500 mmol) were dissolved in deionized water (20 mL). After 30 min of stirring, the pH of the solution was adjusted to 5.5–6.0 using NaOH (3 mol L^{-1}) under stirring. The resulting solution was kept at 80 °C in a water bath for 1 h and then cooled to room temperature and filtered. Slow evaporation at room temperature resulted in colorless square lamellar crystals of **1** after about 1 week, which were filtered off and air dried. The obtained yield: 40% (0.66 g, based on $K_{14}[As_2W_{19}O_{67}(H_2O)]$). Elemental analysis (%) calcd for **1**: C, 0.22; H, 0.75. Found: C, 0.27 and H, 0.70. IR (KBr pellets, cm^{-1}): 3440 (br), 1643 (s), 1320 (w), 947 (s), 885 (s), 795 (s), 733 (s).

Syntheses of $K_{17}Na_2H_5[\{(As_2W_{19}O_{67}(H_2O))Pr(H_2O)_2\}_2(C_2O_4)]\cdot 50H_2O$ (2)

The synthesis of **2** is similar to that of **1**, except that $PrCl_3\cdot 6H_2O$ (0.093 g, 0.25 mmol) replaced $SmCl_3\cdot 6H_2O$ (0.091 g, 0.25 mmol). Green square lamellar crystals of **2** were obtained. The obtained yield: 38% (0.66 g, based on $K_{14}[As_2W_{19}O_{67}(H_2O)]$). Elemental analysis (%) calcd for **2**: C, 0.21; H, 0.76. Found: C, 0.29; H, 0.66. IR (KBr pellets, cm^{-1}): 3441 (br), 1643 (s), 1324 (w), 947 (s), 885 (s), 796 (s), 734 (s).

Syntheses of $K_{17}Na_2H_5[\{(As_2W_{19}O_{67}(H_2O))Ce(H_2O)_2\}_2(C_2O4)]\cdot 50H_2O$ (3)

The synthesis of **3** is similar to that of **1**, except that $CeCl_3\cdot 6H_2O$ (0.093 g, 0.25 mmol) replaced $SmCl_3\cdot 6H_2O$ (0.091 g, 0.25 mmol). Yellow square lamellar crystals for **3** were obtained. The obtained yield: 43% (0.66 g, based on $K_{14}[As_2W_{19}O_{67}(H_2O)]$). Elemental analysis (%) calcd for **3**: C, 0.26; H, 0.81. Found: C, 0.22; H, 0.75. IR (KBr pellets, cm^{-1}): 3424 (br), 1643 (s), 1315 (w), 947 (s), 890 (s), 796 (s), 730 (s).

Conflicts of interest

There are no conflicts to declare.

Acknowledgements

This work was financially supported by the National Natural Science Foundation of China (21771053, 21771054, 21571050 and 21573056), the Henan Province Science and Technology Attack Plan Project (182102210237), the Major Project of Science and Technology, Education Department of Henan Province (20A150010) and the 2020 Students Innovative Pilot Plan of Henan University (202010475086).

Notes and references

1 (*a*) P. Gouzerh and A. Proust, *Chem. Rev.*, 1998, **98**, 77–112; (*b*) Y. P. Jeannin, *Chem. Rev.*, 1998, **98**, 51–76; (*c*) E. Cadot, M. N. Sokolov, V. P. Fedin, C. Simonnet-Jégat, S. Floquet and F. Sécheresse, *Chem. Soc. Rev.*, 2012, **41**, 7335–7353; (*d*) X. López, J. J. Carbó, C. Bo and J. M. Poblet, *Chem. Soc. Rev.*, 2012, **41**, 7537–7571.

2 (*a*) R. Gupta, F. Hussain, M. Sadakane, C. Kato, K. Inoue and S. Nishihara, *Inorg. Chem.*, 2016, **55**, 8292–8300; (*b*) C. Li, N. Mizuno, K. Yamaguchi and K. Suzuki, *J. Am. Chem. Soc.*, 2019, **141**, 7687–7692; (*c*) Y.-F. Song and R. Tsunashima, *Chem. Soc. Rev.*, 2012, **41**, 7384–7402; (*d*) L. Cronin, *Chem. Soc. Rev.*, 2012, **41**, 7333–7334; (*e*) G. Wang, R. Meng, J. Yang, X. He, J. Chen, D. Zhang, X. Xu and J. Niu, *Chem. Commun.*, 2019, **55**, 1619–1622.

3 (*a*) P. Yin, D. Li and T. Liu, *Chem. Soc. Rev.*, 2012, **41**, 7368–7383; (*b*) H. Lv, Y. V. Geletii, C. Zhao, J. W. Vickers, G. Zhu, Z. Luo, J. Song, T. Lian, D. G. Musaev and C. L. Hill, *Chem. Soc. Rev.*, 2012, **41**, 7572–7589; (*c*) D. Li, X. Ma, Q. Wang, P. Ma, J. Niu and J. Wang, *Inorg. Chem.*, 2019, **58**, 15832–15840; (*d*) S.-M. Wang, J. Hwang and E. Kim, *J. Mater. Chem. C*, 2019, **7**, 7828–7850; (*e*) J. He, J. Li, Q. Han, C. Si, G. Niu, M. Li, J. Wang and J. Niu, *ACS Appl. Mater. Interfaces*, 2020, **12**, 2199–2206; (*f*) J. He, Q. Han, J. Li, Z. Shi, X. Shi and J. Niu, *J. Catal.*, 2019, **376**, 161–167; (*g*) Z. Shi, J. Li, Q. Han, X. Shi, C. Si, G. Niu, P. Ma and M. Li, *Inorg. Chem.*, 2019, **58**, 12529–12533; (*h*) Y. Huo, Y.-C. Chen, S.-G. Wu, J.-L. Liu, J.-H. Jia, W.-B. Chen, B.-L. Wang, Y.-Q. Zhang and M.-L. Tong, *Inorg. Chem.*, 2019, **58**, 1301–1308; (*i*) J. T. Rhule, C. L. Hill, D. A. Judd and R. F. Schinazi, *Chem. Rev.*, 1998, **98**, 327–358.

4 (*a*) J. Cuan and B. Yan, *RSC Adv.*, 2014, **4**, 1735–1743; (*b*) M. K. Saini, R. Gupta, S. Parbhakar, A. Kumar Mishra, R. Mathur and F. Hussain, *RSC Adv.*, 2014, **4**, 25357–25364.

5 (*a*) Z. Liang, H. Wu, V. Singh, Y. Qiao, M. Li, P. Ma, J. Niu and J. Wang, *Inorg. Chem.*, 2019, **58**, 13030–13036; (*b*) X. Ma, P. He, B. Xu, J. Lu, R. Wan, H. Wu, Y. Wang, P. Ma, J. Niu and J. Wang, *Dalton Trans.*, 2019, **48**, 12956–12963; (*c*) Y. Huo, R. Wan, P. Ma, J. Liu, Y. Chen, D. Li, J. Niu, J. Wang and M.-L. Tong, *Inorg. Chem.*, 2017, **56**, 12687–12691; (*d*) J.-C. Liu, Q. Han, L.-J. Chen, J. W. Zhao, C. Streb and Y.-F. Song, *Angew. Chem., Int. Ed.*, 2018, **57**, 8416–8420; (*e*) H. Li, Y.-J. Liu, Y.-M. Li, L.-J. Chen, J.-W. Zhao and G.-Y. Yang, *Chem. - Asian J.*, 2018, **13**, 2897–2907; (*f*) R. Gupta, M. K. Saini, F. Doungmene, P. de Oliveira and F. Hussain, *Dalton Trans.*, 2014, **43**, 8290–8299; (*g*) S. Chen, P. Ma, H. Luo, Y. Wang, J. Niu and J. Wang, *Chem. Commun.*, 2017, **53**, 3709–3712; (*h*) L. Ni, F. Hussain, B. Spingler, S. Weyeneth and G. R. Patzke, *Inorg. Chem.*, 2011, **50**, 4944–4955.

6 (*a*) C. Lu, M. Jin, X. Wang, C. Zhai and J. Zhao, *Inorg. Chem. Commun.*, 2018, **88**, 65–69; (*b*) H. Wu, B. Yan, R. Liang, V. Singh, P. Ma, J. Wang and J. Niu, *Dalton Trans.*, 2020, **49**, 388–394; (*c*) P. Ma, F. Hu, H. Wu, X. Liu, J. Wang and J. Niu, *J. Lumin.*, 2020, **217**, 116760.

7 (*a*) J. Zhao, D. Shi, L. Chen, X. Cai, Z. Wang, P. Ma, J. Wang and J. Niu, *CrystEngComm*, 2012, **14**, 2797–2806; (*b*) H. Wu, M. Zhi, H. Chen, V. Singh, P. Ma, J. Wang and J. Niu, *Spectrochim. Acta, Part A*, 2019, **223**, 117294; (*c*) H. Wu, H. Chen, M. Fu, R. Li, P. Ma, J. Wang and J. Niu, *Dyes Pigm.*, 2019, **171**, 107696; (*d*) X. Xu, H. Li, S. Xie, L. Mei, R. Meng, L. Chen and J. Zhao, *Inorg. Chem.*, 2020, **59**, 648–660.

8 (*a*) Q. Han, J. C. Liu, Y. Wen, L. J. Chen, J. W. Zhao and G. Y. Yang, *Inorg. Chem.*, 2017, **56**, 7257–7269; (*b*) Q. Han, Y. Wen, J.-C. Liu, W. Zhang, L.-J. Chen and J.-W. Zhao, *Inorg. Chem.*, 2017, **56**, 13228–13240; (*c*) Y. Li, H. Li, J. Jiang, L. Chen and J. Zhao, *Inorg. Chem.*, 2019, **58**, 3479–3491; (*d*) H. Li, Y. Liu, R. Zheng, L. Chen, J.-W. Zhao and G.-Y. Yang, *Inorg. Chem.*, 2016, **55**, 3881–3893; (*e*) L. Chen, F. Zhang, X. Ma, J. Luo and J. Zhao, *Dalton Trans.*, 2015, **44**, 12598–12612; (*f*) Y. Chen, L. Sun, S. Chang, L. Chen and J. Zhao, *Inorg. Chem.*, 2018, **57**, 15079–15092; (*g*) J. Liu, J. Yu, Q. Han, Y. Wen, L. Chen and J. Zhao, *Dalton Trans.*, 2016, **45**, 16471–16484.

9 (*a*) P. Ma, F. Hu, R. Wan, Y. Huo, D. Zhang, J. Niu and J. Wang, *J. Mater. Chem. C*, 2016, **4**, 5424–5433; (*b*) H. Wu, B. Yan, H. Li, V. Singh, P. Ma, J. Niu and J. Wang, *Inorg. Chem.*, 2018, **57**, 7665–7675; (*c*) H. Li, H. Wu, R. Wan, Y. Wang, P. Ma, S. Li, J. Wang and J. Niu, *Dalton Trans.*, 2019, **48**, 2813–2821; (*d*) H. Wu, R. Wan, Y. Si, P. Ma, J. Wang and J. Niu, *Dalton Trans.*, 2018, **47**, 1958–1965; (*e*) P. Ma, F. Hu, Y. Huo, D. Zhang, C. Zhang, J. Niu and J. Wang, *Cryst. Growth Des.*, 2017, **17**, 1947–1956; (*f*) P. Ma, R. Wan, Y. Si, F. Hu, Y. Wang, J. Niu and J. Wang, *Dalton Trans.*, 2015, **44**, 11514–11523; (*g*) P. Ma, F. Hu, J. Wang and J. Niu, *Coord. Chem. Rev.*, 2019, **378**, 281–309.

10 (*a*) C. Ritchie, E. G. Moore, M. Speldrich, P. Kögerler and C. Boskovic, *Angew. Chem., Int. Ed.*, 2010, **49**, 7702–7705; (*b*) C. Ritchie, V. Baslon, E. G. Moore, C. Reber and C. Boskovic, *Inorg. Chem.*, 2012, **51**, 1142–1151; (*c*) F. Hussain, R. W. Gable, M. Speldrich, P. Kögerler and C. Boskovic, *Chem. Commun.*, 2009, 328–330; (*d*) M. Vonci, F. Akhlaghi Bagherjeri, P. D. Hall, R. W. Gable, A. Zavras, R. A. J. O'Hair, Y. Liu, J. Zhang, M. R. Field, M. B. Taylor, J. Du Plessis, G. Bryant, M. Riley, L. Sorace, P. A. Aparicio, X. López, J. M. Poblet, C. Ritchie and C. Boskovic, *Chem. – Eur. J.*, 2014, **20**, 14102–14111; (*e*) C. Ritchie and C. Boskovic, *Cryst. Growth Des.*, 2010, **10**, 488–491; (*f*) C. Ritchie, M. Speldrich, R. W. Gable, L. Sorace, P. Kögerler and C. Boskovic, *Inorg. Chem.*, 2011, **50**, 7004–7014; (*g*) C. Ritchie, C. E. Miller and C. Boskovic, *Dalton Trans.*, 2011, **40**, 12037–12039; (*h*) C. Ritchie, E. G. Moore, M. Speldrich, P. Kögerler and C. Boskovic, *Angew. Chem.*, 2010, **122**, 7868–7871.

11 (*a*) C. Tourné, A. Revel, G. Tourné and M. Vendrell, *C. R. Hebd. Seances Acad. Sci., Ser. C*, 1973, **277**, 643–645; (*b*) U. Kortz, M. G. Savelieff, B. S. Baassil and M. H. Dickman, *Angew. Chem., Int. Ed.*, 2001, **40**, 3384–3386.

12 (*a*) F. Hussain, F. Conrad and G. Patzke, *Angew. Chem., Int. Ed.*, 2009, **48**, 9088–9091; (*b*) H. Chen, L. Sun, J. Zhang,

Z. Xiao, P. Ma, J. Wang, Y. Zhang and J. Niu, *Dalton Trans.*, 2020, **49**, 12458–12465; (*c*) Q. Han, X. Sun, J. Li, P. Ma and J. Niu, *Inorg. Chem.*, 2014, **53**, 2006–2011; (*d*) J. Zhao, D. Shi, L. Chen, P. Ma, J. Wang and J. Niu, *CrystEngComm*, 2011, **13**, 3462–3469; (*e*) F. Hussain and U. Kortz, *Chem. Commun.*, 2005, **9**, 1191–1193; (*f*) Y. Huo, Z. Huo, P. Ma, J. Wang and J. Niu, *Inorg. Chem.*, 2015, **54**, 406–408; (*g*) Y. Niu, Q. Xu, Y. Wang, Z. Li, J. Lu, P. Ma, C. Zhang, J. Niu and J. Wang, *Dalton Trans.*, 2018, **47**, 9677–9684.

13 W. Liu and H. H. Thorp, *Inorg. Chem.*, 1993, **32**, 4102–4105.

14 (*a*) P. Mialane, J. Marrot, A. Mallard and G. Hervé, *Inorg. Chim. Acta*, 2002, **328**, 81–86; (*b*) F. Hussain, U. Kortz and R. J. Clark, *Inorg. Chem.*, 2004, **43**, 3237–3241; (*c*) F. Hussain, B. S. Bassil, U. Kortz, O. A. Kholdeeva, M. N. Timofeeva, P. Oliveira, B. Keita and L. Nadjo, *Chem. – Eur. J.*, 2007, **13**, 4733–4742; (*d*) A. H. Ismail, B. S. Bassil, I. Römer, N. C. Redeker and U. Kortz, *Z. Naturforsch.*, 2010, **65b**, 383–389.

15 (*a*) M. Llunell, D. Casanova, J. Cirera, J. M. Bofill, P. Alemany, S. Alvarez, M. Pinsky and D. Avnir, *SHAPE V2.1*, Universitat de Barcelona, 2013; (*b*) S. Alvarez, *Dalton Trans.*, 2013, **42**, 8617–8636.

16 (*a*) S. Zhang, Y. Wang, J. Zhao, P. Ma, J. Wang and J. Niu, *Dalton Trans.*, 2012, **41**, 3764–3772; (*b*) X. Wang, Y. Liu, M. Jin, Y. Wu, L. Chen and J.-W. Zhao, *Cryst. Growth Des.*, 2017, **17**, 5295–5308; (*c*) J. Zhao, H. Li, Y. Li, C. Li, Z. Wang and L. Chen, *Cryst. Growth Des.*, 2014, **14**, 5495–5505.

17 (*a*) D. Zhang, S. Zhang, P. Ma, J. Wang and J. Niu, *Inorg. Chem. Commun.*, 2012, **20**, 191–195; (*b*) S. Zhang, J. Zhao, P. Ma, J. Niu and J. Wang, *Chem. – Asian J.*, 2012, **7**, 966–974; (*c*) F. Li, W. Guo, L. Xu, L. Ma and Y. Wang, *Dalton Trans.*, 2012, **41**, 9220–9226; (*d*) C. Den Auwer, M. C. Charbonnel, M. G. B. Drew, M. Grigoriev, M. J. Hudson, P. B. Iveson, C. Madic, M. Nierlich, M. T. Presson, R. Revel, M. L. Russell and P. Thuéry, *Inorg. Chem.*, 2000, **39**, 1487–1495.

18 (*a*) I. E. Wachs and C. A. Roberts, *Chem. Soc. Rev.*, 2010, **39**, 5002–5017; (*b*) H. Wu, M. Zhi, C. Chen, Y. Zhu, P. Ma, J. Wang and J. Niu, *Dalton Trans.*, 2019, **48**, 13850–13857.

19 (*a*) J. Wang, P. Ma, S. Li, Q. Xu, Y. Li, J. Niu and J. Wang, *Inorg. Chem.*, 2019, **58**, 57–60; (*b*) H. Li, W. Yang, X. Wang, L. Chen, J. Ma, L. Zheng and J. Zhao, *Cryst. Growth Des.*, 2016, **16**, 108–120.

20 (*a*) I. I. Kindrat, B. V. Padlyak, B. Kukliński, A. Drzewiecki and V. T. Adamiv, *J. Lumin.*, 2019, **213**, 290–296; (*b*) S. Damodaraiah and Y. C. Ratnakaram, *J. Lumin.*, 2019, **207**, 553–560; (*c*) H. An, Y. Zhang, Y. Hou, T. Hu, W. Yang, S. Chang and J. Zhang, *Dalton Trans.*, 2018, **47**, 9079–9089; (*d*) M. Zhao, Y. Liu, S. Ma, D. Liu and K. Wang, *J. Lumin.*, 2018, **202**, 57–64; (*e*) B. Artetxe, S. Reinoso, L. San Felices, L. Lezama, J. M. Gutiérrez-Zorrilla, J. A. García, J. R. Galán-Mascarós, A. Haider, U. Kortz and C. Vicent, *Chem. – Eur. J.*, 2014, **20**, 12144–12156.

21 (*a*) J.-C. G. Bünzli and C. Piguet, *Chem. Soc. Rev.*, 2005, **34**, 1048–1077; (*b*) K. Binnemans, *Chem. Rev.*, 2009, **109**, 4283–4374; (*c*) J.-C. G. Bünzli, *Chem. Rev.*, 2010, **110**, 2729–2755; (*d*) S. V. Eliseeva and J.-C. G. Bünzli, *Chem. Soc. Rev.*, 2010, **39**, 189–227; (*e*) E. G. Moore, A. P. S. Samuel and K. N. Raymond, *Acc. Chem. Res.*, 2009, **42**, 542–552; (*f*) M. Shang, C. Li and J. Lin, *Chem. Soc. Rev.*, 2014, **43**, 1372–1386; (*g*) P. Mahata, K. V. Ramya and S. Natarajan, *Chem. – Eur. J.*, 2008, **14**, 5839–5850.

22 (*a*) X. Xu, Y. Chen, Y. Zhang, Y. Liu, L. Chen and J. Zhao, *Inorg. Chem.*, 2019, **58**, 11636–11648; (*b*) H.-L. Li, Y.-J. Liu, J.-L. Liu, L.-J. Chen, J.-W. Zhao and G.-Y. Yang, *Chem. – Eur. J.*, 2017, **23**, 2673–2689; (*c*) T. Yamase, *Chem. Rev.*, 1998, **98**, 307–326; (*d*) H. Wu, M. Zhi, V. Singh, H. Li, P. Ma, J. Niu and J. Wang, *Dalton Trans.*, 2018, **47**, 13949–13956.